

# Gland Instance Segmentation Using Deep Multichannel Neural Networks

Yan Xu<sup>a,b</sup>, Yang Li<sup>a</sup>, Yipei Wang<sup>a</sup>, Mingyuan Liu<sup>a</sup>, Yubo Fan<sup>a</sup>, Maode  
Lai<sup>c</sup>, Eric I-Chao Chang<sup>b,\*</sup>

<sup>a</sup>*State Key Laboratory of Software Development Environment and Key Laboratory of  
Biomechanics and Mechanobiology of Ministry of Education and Research Institute of  
Beihang University in Shenzhen, Beihang University, Beijing 100191, China*

<sup>b</sup>*Microsoft Research, Beijing 100080, China*

<sup>c</sup>*Department of Pathology, School of Medicine, Zhejiang University, Hangzhou 310058,  
China*

---

## Abstract

We propose a new image instance segmentation method that segments individual glands (instances) in colon histology images. This process is challenging since the glands not only need to be segmented from a complex background, they must also be individually identified. We leverage the idea of image-to-image prediction in recent deep learning by designing an algorithm that automatically exploits and fuses complex multichannel information - regional, location and boundary cues - in gland histology images. Our proposed algorithm, a deep multichannel framework, alleviates heavy feature design due to the use of convolutional neural networks and is able to meet multifarious requirements by altering channels. Compared to methods reported in the 2015 MICCAI Gland Segmentation Challenge and other currently prevalent instance segmentation methods, we observe state-of-the-art results based on the evaluation metrics.

*Keywords:* Instance segmentation, convolutional neural network, segmentation, multichannel, histology image.

---

\*Corresponding author

*Email address:* [echang@microsoft.com](mailto:echang@microsoft.com) (Eric I-Chao Chang)

## 1. Introduction

Existing in most organ systems as important structures, glands secrete proteins and carbohydrates. However, adenocarcinomas, the most prevalent type of cancer, arises from the glandular epithelium (Travis et al., 2011). The morphology of glands determines whether they are benign or malignant and the level of severity (Nguyen et al., 2012b). Segmenting glands from the background tissue is important for analyzing and diagnosing histological images.

In gland labeling/segmentation, each pixel is assigned one label to represent whether the pixel belongs to the foreground (gland) or the background. However, which gland the foreground pixel belongs to is still not determined. In order to analyze the morphology of glands, they need to be recognized individually. Each pixel needs to be classified and it must be determined which gland the pixel belongs to, which is to assign a gland ID to each foreground pixel. We call this task as **gland instance segmentation** (as shown in Fig.1). In this paper, we aim to solve the gland instance segmentation problem. We formulate this problem as two sub-problems - gland labeling/segmentation and instance recognition.

The intrinsic properties of gland histopathological image pose plenty of challenges in instance segmentation (Dimopoulos et al., 2014). First of all, heterogeneous shapes make it difficult to use mathematical shape models to achieve segmentation. As Fig.1 shows, the cytoplasm being filled with mucinogen granule causes the nucleus to be extruded into a flat shape whereas the nucleus appears as a round or oval body after secreting. Second, variability of intra- and extra- cellular matrices often leads to anisochromasia. Therefore, the background portion of histopathological images contains more noise like intensity gradients, compared to natural images. Several problems arise in our exploration of analyzing gland images: 1) some objects are very close together making only the tiny gaps between them visible when zooming in on a particular image area; or 2) one entity borders another making their edges adhesive to each other. We call this an issue of '*coalescence*'. If these issues are omitted during instance recognition process, even if there is only one pixel coalescing with another, the algorithm will consider two instances as one.

Gland labeling/segmentation, as one sub-problem of gland instance segmentation, is a well-studied field in which various methods have been explored, such as morphology-based methods (Naik et al., 2007; Nguyen et al.,

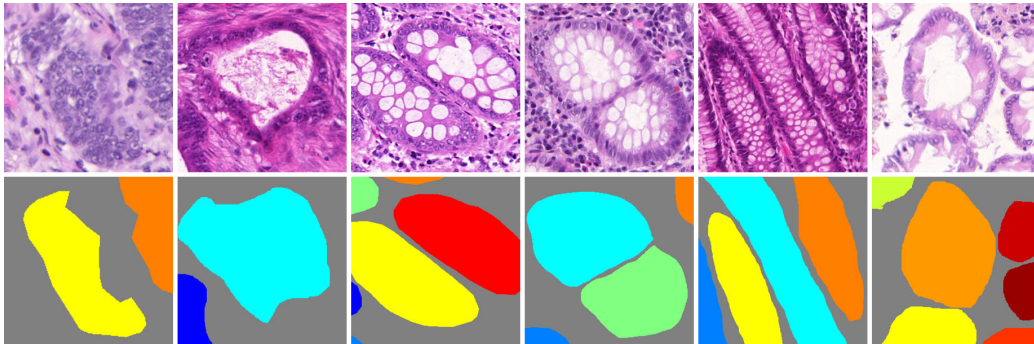


Figure 1: Gland Haematoxylin and Eosin (H&E) stained slides and ground truth labels. Images in the first row exemplify different glandular structures. Characteristics such as heterogeneousness and anisochromasia can be observed in this figure. The second row shows the ground truth. To achieve better visual effects, each color represents an individual glandular structure.

2010; Naik et al., 2008; Paul and Mukherjee, 2016) and graph-based methods (Egger, 2013; Tosun and Gunduz-Demir, 2011). However, glands must be recognized individually to enable the following morphology analysis. Gland segmentation is insufficient due to its inability to recognize each gland in histopathological images. The MICCAI 2015 Gland Segmentation Challenge Contest (Sirinukunwattana et al., 2017) has drawn attention to gland instance segmentation. The precise gland instance segmentation in histopathological images is essential for morphology assessment, which has been proven to be not only a valuable tool for clinical diagnosis but also a prerequisite for cancer grading (Fleming et al., 2012).

Although gland instance segmentation is a relatively new subject, instance segmentation in nature images has attracted much interest from researchers. Ever since SDS (Hariharan et al., 2014) raised this problem and proposed a basic framework to solve it, other methods have been proposed thereafter, such as hypercolumn (Hariharan et al., 2015) and MNC (Dai et al., 2016b), which merely optimize and accelerate the feature extraction process. All of these algorithms fall into a routine that detects objects first and then segments object instances inside the detected bounding boxes.

In medical image analysis, traditional methods are more prevalent for segmenting gland instances instead of learning-based methods. Traditional methods depend heavily on hand-craft features and prior knowledge. In natural images, instance segmentation algorithms are mostly the pipeline

of object detection and masking (Hariharan et al., 2014, 2015; Dai et al., 2016b). The objects in natural images are regular-shaped, and relatively easy to segment by first creating bounding boxes for each one. However, most glands are irregular in shape, which increases the difficulty of detecting the whole gland structure. Thus the traditional instance segmentation methods for natural images are not suitable for gland instance segmentation.

In a broad sense, gland instance segmentation can be viewed as gland labeling process with commutative labels. Thus gland labeling can offer useful cues for gland instance segmentation. The latest advantages in deep learning technologies have led to explosive growth in machine learning and computer vision for building systems that have shown significant improvements in a huge range of applications such as image classification (Krizhevsky et al., 2012; Simonyan and Zisserman, 2015) and object detection (Girshick, 2015). The fully convolutional neural networks (FCN) (Long et al., 2015) permit end-to-end training and testing for image labeling; HED (Xie and Tu, 2015) detector learns hierarchically embedded multi-scale edge fields to account for the low-, mid-, and high- level information for contours and object boundaries; Faster R-CNN (Ren et al., 2015) predicts object locations and compensates for the possible failure of edge prediction. We solve the gland instance segmentation problem by multi-task learning. One task is to segment the gland images, and another task is to identify the gland instances. In the gland segmentation sub-task, a fully convolutional neural network (FCN) (Long et al., 2015) model is employed to exploit the advantage of end-to-end training and image-to-image prediction. In the gland instance recognition sub-task, a holistically-nested edge detector (HED) and a faster R-CNN object detector are applied to define the instance boundaries.

We make use of multichannel learning to extract region, boundary and location cues and solve the instance segmentation issue in gland histology images (as shown in Fig. 2). Our algorithm is evaluated on the dataset provided by the MICCAI 2015 Gland Segmentation Challenge Contest (Sirinukunwattana et al., 2017) and achieves state-of-the-art performance among all participants and other popular methods of instance segmentation. We conduct a series of ablation experiments and prove the superiority of the proposed algorithm.

This paper is arranged as follows. We formulate the instance segmentation problem in Section 2. Section 3 is a review of related previous works. In section 4, we describe the complete methodology of the proposed algorithm of gland instance segmentation. Section 5 is a detailed evaluation of our

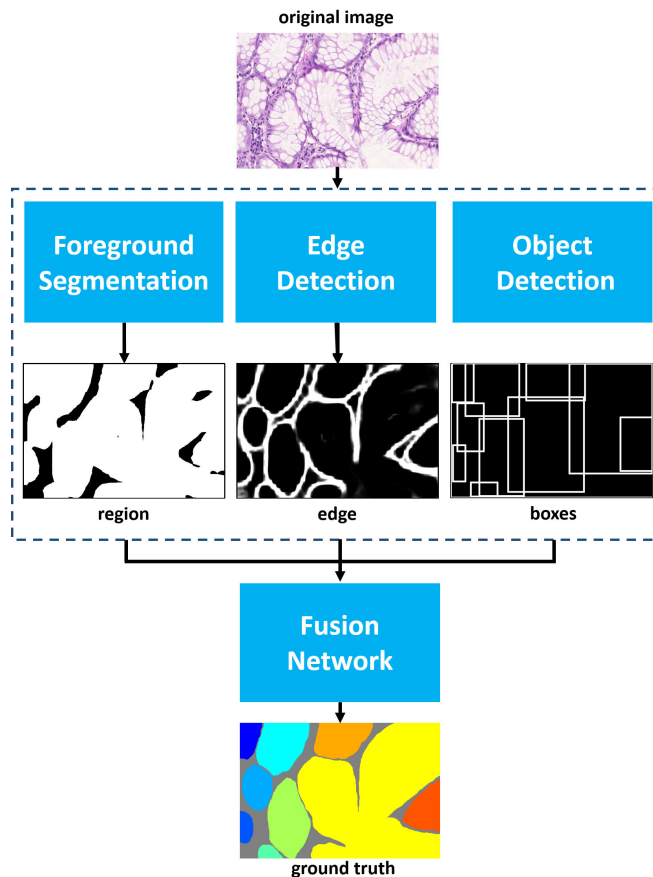


Figure 2: This illustrates a brief structure of the proposed algorithm. The foreground segmentation channel distinguishes gland pixels from the background. The edge detection channel outputs the result of boundary detection. The object detection channel detects glands and their regions in the images. A convolution neural network concatenates features generated by different channels and produces segmented instances. The white areas in sub-image "region", "edge" and "boxes" represent the results of the recognized glands, edges and detected bounding boxes.

method. Section 6 summarizes our conclusion.

## 2. Problem

We formulate the instance segmentation problem by two sub-problems, labeling/segmentation and instance recognition.

We denote  $D = \{(X_n, Y_n, Z_n), n = 1, 2, \dots, N\}$  as the input training dataset, where  $N$  is the image amount. We subsequently drop the subscript  $n$  for notational simplicity, since we consider each image independently.  $X = \{x_j, j = 1, 2, \dots, |X|\}$  denotes the raw input image,  $Y = \{y_j, j = 1, 2, \dots, |X|\}, y_j \in \{0, 1\}$  denotes the corresponding segmentation label and  $Z = \{R_k, k = 0, 1, 2, \dots, K\}$  denotes the instance label, in which  $R_k = \{(p, q)\}$  denotes the coordinates set of pixels inside of region  $R_k$ . When  $k$  equals 0, it denotes the background area and it denotes the corresponding instance when  $k$  takes other values.  $K$  is the total instance number. Regions in the image satisfy the following relations:

$$R_k \cap R_t = \emptyset, \forall k \neq t \quad (1)$$

$$\cup R_k = \Omega \quad (2)$$

Note that instance labels only count gland instances thus they are commutative. Our objective is to segment glands while ensuring that all instances are differentiated. In the labeling/segmentation sub-problem,  $\hat{Y}$  represents the labeling/segmentation result. The cost function is:

$$Dist(Y, \hat{Y}) = \frac{1}{|Y|} \sum_{j=1}^{|Y|} \delta(y_j \neq \hat{y}_j) \quad (3)$$

In the instance recognition sub-problem,  $\hat{Z}$  denotes the instance prediction. The cost function is:

$$Dist(Z, \hat{Z}) = 1 - \frac{1}{K} \sum_{k'=0}^{K'} L(\widehat{R}_{k'}, Z) \quad (4)$$

where

$$L(\widehat{R}_{k'}, Z) = \begin{cases} 1, & \exists k \neq 0, \frac{\widehat{R}_{k'} \cap R_k}{\widehat{R}_{k'} \cup R_k} \geq T \\ 0, & \text{otherwise} \end{cases}$$

$\widehat{R}_{k'} \in \hat{Z}$  denotes the instance segmentation prediction region and  $R_k \in Z$  denotes the instance label region.  $K'$  represents the total predicted region

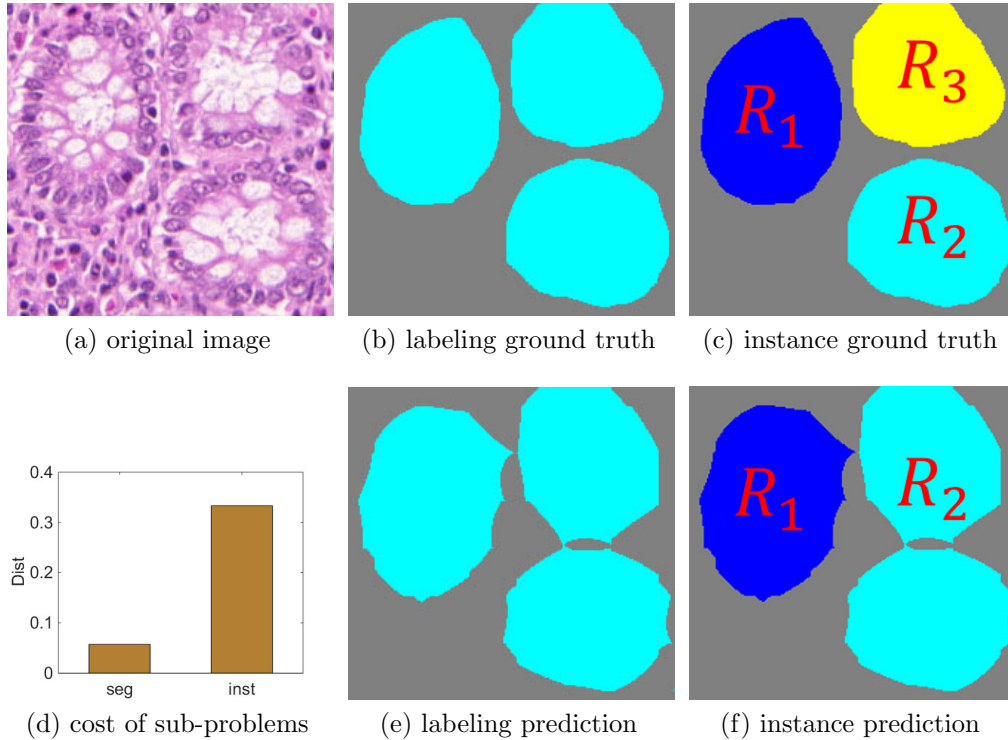


Figure 3: This illustrates two sub-problems of gland instance segmentation. Gland instance segmentation can be formulated into foreground labeling/segmentation and gland instance recognition two sub-problems. For the foreground labeling/segmentation sub-problem, a small amount of prediction errors has little influence on the final cost function; however, for the gland instance recognition sub-problem, even a few pixels predicted incorrectly can highly increase the cost.

count.  $T$  is the threshold which is set to 0.5 in this algorithm. When the overlap ratio of the gland instance in a certain prediction region and labels is higher than the threshold, this region is considered an instance prediction by the algorithm. Fig.3 shows the two gland instance segmentation sub-problems.

Since the cost function of instance recognition is nondifferentiable, it cannot be trained with SGD. We hereby approximate instance recognition by edge detection and object detection. We generate edge labels  $E$  and object labels  $O$  through  $Y$  and  $Z$  to train edge detector and object detector, in

which  $E = \{e_j, j = 1, 2, \dots, |X|\}, e_j \in \{0, 1\}$  and  $e_j$  equals 0 when all four nearest pixels (over, below, right and left) belong to the same instance.  $O$  denotes the smallest bounding box for each gland instance.

### 3. Related Work

This section is a retrospective introduction about instance segmentation and gland instance segmentation.

#### 3.1. Instance segmentation

Instance segmentation, a task requiring distinguishment of contour, location, class and the number of objects in an image, is attracting more and more attention from researchers in image processing and computer vision. As a complex problem can hardly be solved using traditional algorithms, a growing number of deep learning approaches have emerged to solve it. For example, SDS (Hariharan et al., 2014) uses a framework that resembles R-CNN (Girshick et al., 2014) to extract features from both the bounding box of the region and the region foreground, and then classifies region proposals and refines the segmentation inside bounding boxes based on those extracted features. Hypercolumn (Hariharan et al., 2015) defines pixel features as a vector of activations of all CNN units above that pixel, and then classifies region proposals and refines region segmentation based on those feature vectors. MNC (Dai et al., 2016b) integrates three networks designed for detection, segmentation and classification respectively in a cascaded structure. Unlike SDS and Hypercolumn, MNC is capable of training in an end-to-end fashion, since MNC takes advantage of the Region Proposal Network (RPN) to generate region proposals. Similar to SDS and hypercolumn, MNC performs segmentation inside the proposal box as well. In contrast to the above methods, our method performs segmentation and instance recognition in a parallel manner.

#### 3.2. Gland instance segmentation

Gland morphology and structure can vary significantly, which poses a big challenge in gland instance segmentation. Researchers have come up with several methods to solve this problem. Previous works focus on detecting gland structure like nuclei and lumen. Sirinukunwattana et al. (Sirinukunwattana et al., 2015) model every gland as a polygon in which the vertices are located at the nucleus. Cheikh et al. (Cheikh et al., 2016) propose a



mathematical morphology method to characterize the spatial distribution of nuclei in histological images. Nguyen et al. (Nguyen et al., 2012a) use texture and structural features to classify the basic components of glands, and then segment gland instance based on prior knowledge of gland structure. These methods perform well in benign images but are comparatively unsatisfactory when used on malignant images, which has been the impetus for creating methods based on deep learning (Sirinukunwattana et al., 2015). Li et al. (Li et al., 2016) train a window-based binary classifier to segment glands using both CNN features and hand-crafted features. Kainz et al. (Kainz et al., 2015) train two separated networks to recognize glands and gland-separating structures respectively. In the MICCAI 2015 gland segmentation challenge contest, some teams achieved impressive performance. DCAN (Chen et al., 2016) is a multi-task learning framework that combines a down-sampling path and an up-sampling path together. From the hierarchical layer, the framework is separated into two branches to generate contour information and segment objects. Team ExB (Sirinukunwattana et al., 2017) proposes a multi-path convolutional neural network segmentation algorithm. Each path consists of different convolutional layers and is designed to capture different features. All paths are fused by two fully connected layers to integrate information. Team Freiburg (Sirinukunwattana et al., 2017) utilizes an off-the-shelf deep convolutional neural network U-net (Ronneberger et al., 2015), and then performs post-processing of hole-filling and removes objects less than 100 pixels wide from the final results.

### *3.3. Previous work*

An earlier conference version of our approach was presented in Xu et al. (Xu et al., 2016). Here we further illustrate that: (1) we explore another channel - object detection - in this paper, due to the edge detection and the object detection channels complementing each other; (2) ablation experiments are carried out to corroborate the effectiveness of the proposed algorithm; (3) based on the rotation invariance of histological images, a new data augmentation strategy is proposed that has proven to be effective; (4) this algorithm achieves state-of-the-art results on the dataset provided by the 2015 MICCAI Gland Segmentation Challenge Contest.

## 4. Method

There are two possible failures for gland instance segmentation. Since the gland-separating tissues are relatively few and similar to glands in coloration, it is very difficult for segmentation to rule out those pixels completely. Although it has little effect on segmentation, it is detrimental to the instance recognition process. Only one pixel that connects two glands can mislead the algorithm into recognizing that they belong to the same gland. Another possible scenario is that algorithms designed to recognize instances separately may cause prediction areas to be smaller than the ground truth. In this case, the objects number and position may be accurate, but the segmentation performance is substandard. Those two scenarios are illustrated in Fig. 4.

We propose a new multichannel algorithm to achieve gland segmentation and gland instance recognition simultaneously. Our algorithm consists of three channels each designed to undertake different responsibilities. Fig. 2 presents the flow chart of the proposed algorithm. One channel is designed to segment foreground pixels from background pixels. The other two channels are used to recognize instances. Aiming to determine which gland each foreground pixel belongs to, we utilize both object detection and edge detection to define the spatial limits of every gland. The reason for choosing these two channels is based on the fact that information on contour and location contributes respectively and complementarily to instance recognition and the joint effort will perform much better together than each one alone. Specifically, edge detection performs a little better than object detection in instance recognition, but edge detection fails to complete the task because of the coalescence phenomenon of glands as abovementioned, which affects not only segmentation but edge detection as well. Gland detection may perform well for benign and well-shaped glands, but hardly detect the entire glands accurately for malignant ones. However, edge detection and object detection can compensate for each other’s weaknesses and identify instances better. By integrating the information generated from different channels, our multichannel framework is capable of instance segmentation. A detailed depiction of our algorithm is presented in Fig. 5.

### 4.1. Foreground Segmentation Channel

The foreground segmentation channel distinguishes glands from the background.

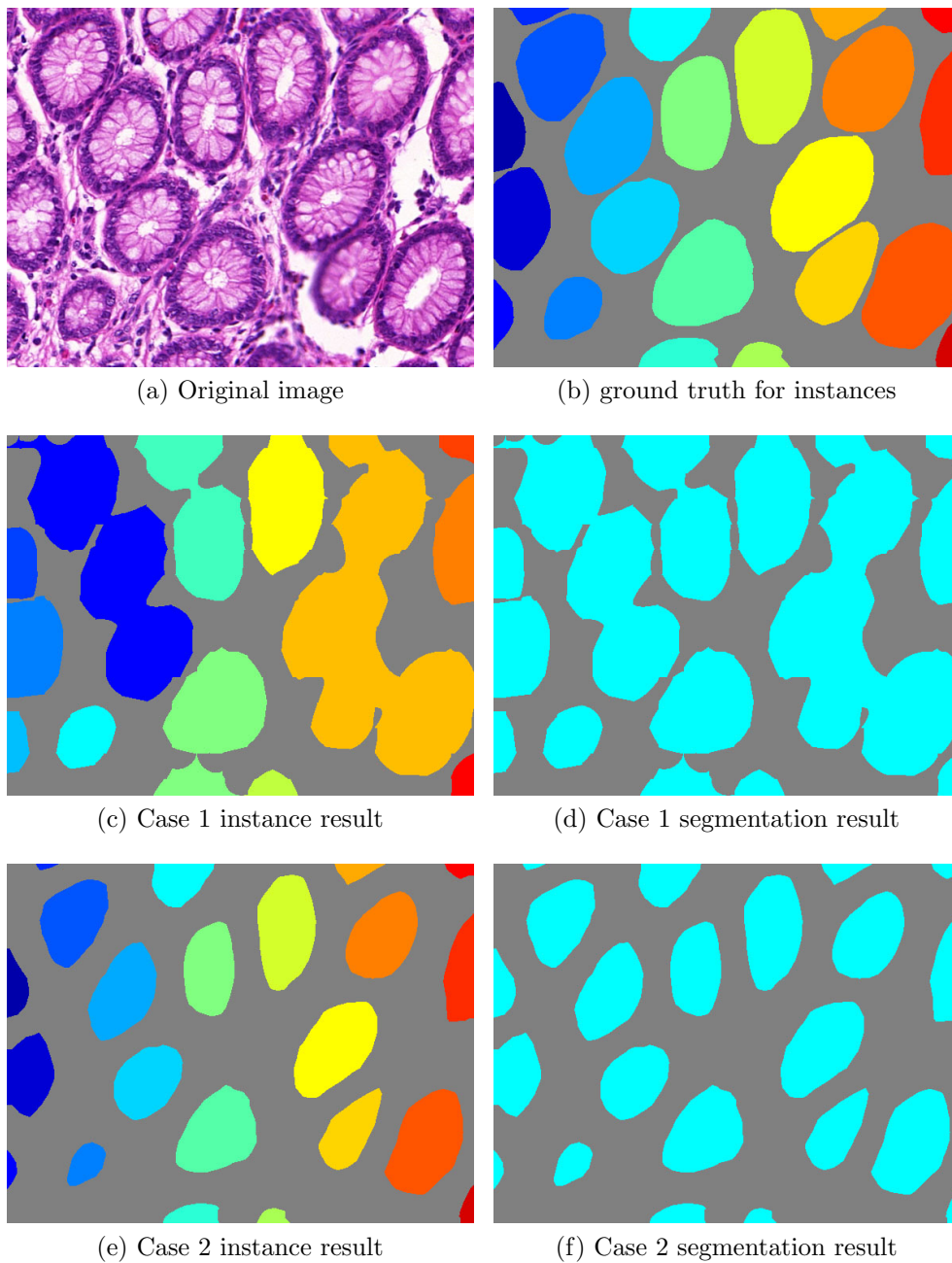


Figure 4: Two possible failures of gland instance segmentation. In the instance results and the ground truth images, different color regions represent different gland instances. Case 1 and Case 2 are two possible scenarios in which the algorithm fails to segment gland instances. In Case 1, glands are separated from the background but instances are not recognized. In Case 2, instances are labeled yet under the condition of many gland pixels being neglected.

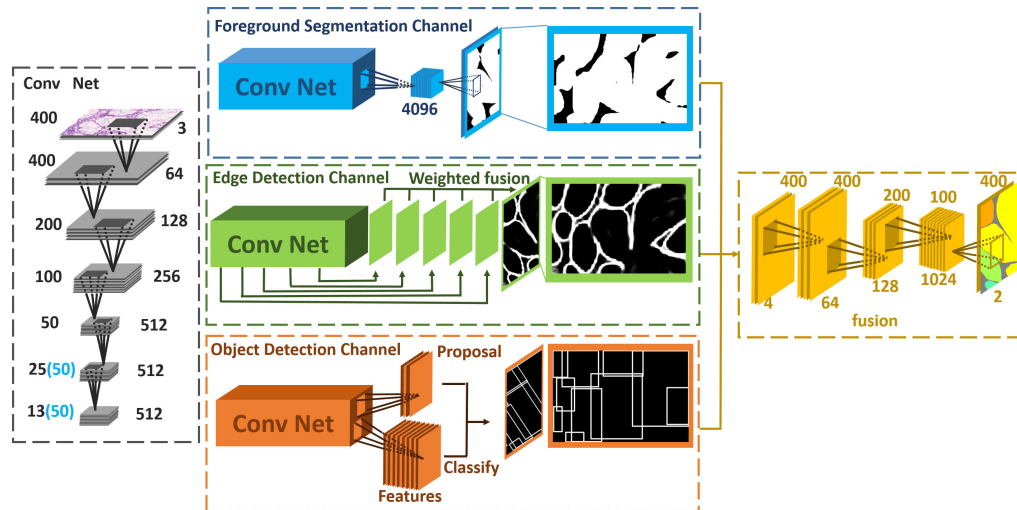


Figure 5: This illustrates the structure of this algorithm. For all the channels in this algorithm, FCN for the foreground segmentation channel, Faster R-CNN (Ren et al., 2015) for the object detection channel and HED the for edge detection channel, are all based on the VGG16 model, we present this classical five pooling structure in detail by "Conv Net" at the left side of the figure and represent it as a rectangular block named "Conv Net". Especially in foreground segmentation and object detection channels, arrows pointing from "Conv Net" denote the output of the "Conv Net", while in the edge detection channel they represent the output of deep supervisions. In the foreground segmentation channel, strides of the last two pooling layers of "Conv Net" are set as 1; dilated convolution is applied to convolution layers leading to the higher resolution of feature maps (as annotated in brackets).

The well-suited solutions to image labeling/segmentation in which each pixel is assigned a label from a pre-specified set are FCN family models (Long et al., 2015; Xie and Tu, 2015). FCN replaces the fully-connected layer with a convolutional layer and upsamples the feature map to the same size as the original images through deconvolution thus an end-to-end training and prediction is guaranteed. Compared to the previous prevalent method, sliding window (Sermanet et al., 2013; Ciresan et al., 2012) in image segmentation, FCN is faster and simpler. Usually, an FCN model can be regarded as the combination of a feature extractor and a pixel-wise predictor. A pixel-wise predictor predicts probability masks of segmented images. The feature

extractor is able to abstract high-level features by down-sampling and convolution. Though useful high-level features are extracted, details of images sink in the process of max-pooling and strided convolution. Consequently, when objects are adjacent to each other, FCN may consider them as one. Applying FCN to segment images is a logical choice but instance segmentation is beyond the ability of FCN. It requires an algorithm to differentiate instances of the same class even when they are extremely close to each other. Even so, probability masks produced by FCN still offer valuable support in solving instance segmentation problems.

To compensate for the resolution reduction of feature maps due to down-sampling, FCN introduces skip architecture to combine deep semantic information and shallow appearance information. Nevertheless, Yu et al. (Yu and Koltun, 2016) propose the dilated convolution that empowers the network with a wider receptive field without downsampling. Less downsampling means less space-invariance brought by downsampling which is beneficial to increasing segmentation precision.

Our foreground segmentation channel is a modified version of the FCN-32s (Long et al., 2015) of which the strides of pool4 and pool5 are 1 and subsequent convolution layers enlarge the receptive field with a dilated convolution.

Given an input image  $X$  and the parameter of the FCN network is denoted as  $w_s$ , thus the output of FCN is

$$P_s(Y^* = k | X; w_s) = \mu_k(h_s(X, w_s)), \quad (5)$$

where  $\mu(\cdot)$  is the softmax function.  $\mu_k(\cdot)$  is the output of the  $k$ th category and  $h_s(\cdot)$  outputs the feature map of the hidden layer.  $Y^*$  is the segmentation prediction.

#### 4.2. Edge Detection Channel

The edge detection channel detects boundaries between glands.

To receive precise and clear boundaries, edges are crucial as proven by DCAN (Chen et al., 2016). The effectiveness of edges in our algorithm can be shown in two ways. First, the edge compensates for the information loss caused by max-pooling and strided convolution in FCN. As a result, contours become more precise and the morphology becomes more similar to the ground truth. Second, even if the location and the probability mask are confirmed, it is unavoidable that predicted pixel regions of adjacent objects

are still connected. Edge, however, is able to differentiate between them. As expected, the synergy of regions, locations and edges achieves state-of-the-art results. The edge channel in our model is based on a Holistically-nested Edge Detector (HED) (Xie and Tu, 2015). It is a CNN-based solution towards edge detection. It learns hierarchically embedded multi-scale edge fields to account for the low-, mid-, and high- level information of contours and object boundaries. In edge detection, pixels of labels are much less than pixels of backgrounds. The imbalance may decrease the convergence rate or even cause the non-convergence problem. To solve the problem, deep supervision (Lee et al., 2015) is deployed. In total, there are five side supervisions which are established before each down-sampling layer.

We denote  $w_e$  as the parameter of HED, thus the  $m$ th prediction of deep supervision is

$$P_e^{(m)}(E^{(m)*} = 1 | X; w_e) = \sigma(h_e^{(m)}(X, w_e)). \quad (6)$$

$\sigma(\cdot)$  denotes the sigmoid function - the output layer of HED.  $h_e^{(m)}$  represents the output of the hidden layer relative to  $m$ th deep supervision and  $E^{(m)*}$  denotes the  $m$ th side output prediction. The weighted sum of  $M$  outputs of deep supervision is the final result of this channel which is denoted as  $E^*$ , and the weighted coefficient is  $\alpha$ .

$$P_e(E^* = 1 | X; w_e, \alpha) = \sigma\left(\sum_{m=1}^M \alpha^{(m)}, h_e^{(m)}(X, w_e)\right) \quad (7)$$

This process is delivered through the convolutional layer. The back propagation enables the network to learn relative levels of importance of edge predictions under different scales.

### 4.3. Object Detection Channel

The object detection channel detects glands and their locations in the image.

Object detection is helpful in counting and identifying the range of objects. According to some previous works on instance segmentation, such as MNC (Dai et al., 2016a), confirmation of the bounding-box is usually the first step in instance segmentation. After that, segmentation and other options are carried out within bounding boxes. Though this method is widely recognized, the loss of context information caused by the limited receptive

field of bounding-box may exacerbate segmentation results. Consequently, we integrate location information into the fusion network instead of segmenting instances within bounding boxes. To obtain location information, Faster R-CNN, a state-of-the-art object detection model, is conceived. Convolutional layers are applied to extract feature maps from images. After that, the Region Proposal Network (RPN) takes an arbitrary-sized feature map as input and produces a set of bounding-boxes with the probability of objects. Region proposals will be converted into regions of interest and classified to form the final object detection result.

Filling is done in order to transform the bounding box prediction into a new formation that represents the number of bounding boxes that every pixel belongs to. The value of each pixel in regions covered by the bounding boxes equals the number of bounding boxes it belongs to. For example, if a pixel is in the overlapping area of three bounding boxes, the value of that pixel will be three.

$w_d$  is denoted as the parameter of Faster R-CNN and  $\phi$  represents the filling operation. The output of this channel is

$$P_d(X, w_d) = \phi(h_d(X, w_d)). \quad (8)$$

$h_d(\cdot)$  is the predicted coordinate of the bounding box.

#### 4.4. Fusing Multichannel

Merely receiving the information of these three channels is not the ultimate purpose of our algorithm. As a result, a fusion algorithm is of great importance to maximize synergies of the three kinds of information - region, location and boundary cues. It is hard for an algorithm which is not learning-based to recognize the patterns of all this information. Naturally, a CNN based solution is the best choice.

After obtaining outputs of these three channels, a shallow seven-layer convolutional neural network is used to combine information and yield the final result. To reduce information loss and ensure a sufficiently large reception field, we again replace downsampling with dilated convolution.

We denote  $w_f$  as the parameter of this network and  $h_f$  as the hidden layer. Thus the output of the network is

$$P(Y_I^* = k \mid P_s, P_d, P_e; w_f) = \mu_k(h_f(P_s, P_d, P_e, w_f)). \quad (9)$$

$Y_I^*$  is the instance segmentation prediction.

## 5. Experiment

### 5.1. Dataset

Our method is evaluated on the dataset provided by the MICCAI 2015 Gland Segmentation Challenge Contest (Sirinukunwattana et al., 2017). The dataset consists of 165 labeled colorectal cancer histological images scanned by Zeiss MIRAX MIDI. The image resolution is approximately 0.62m per pixel. 85 images belong to the training set and 80 are part of test sets (test set A contains 60 images and test set B contains 20 images). There are 37 benign sections and 48 malignant ones in the training set, 33 benign sections and 27 malignant ones in testing set A and 4 benign sections and 16 malignant ones in testing set B.

### 5.2. Data augmentation and Preprocessing

We first preprocess data by performing per channel zero mean. The next step is to generate edge labels from region labels and perform dilation on edge labels afterwards. Whether a pixel is an edge or not is decided by its four nearest pixels (over, below, right and left) in the region label. If all four pixels in the region label belong to the foreground or in the background, this pixel does not belong to any edge. To enhance performance and combat overfitting, copious amounts of training data are needed. Given the circumstance of the absence of a large dataset, data augmentation is essential before training. Two strategies for data augmentation have been carried out and the improvement of results is strong enough evidence to prove the efficiency of data augmentation. In Strategy I, horizontal flipping and rotation operation ( $0^\circ$ ,  $90^\circ$ ,  $180^\circ$ ,  $270^\circ$ ) are used in training images. Besides operations in Strategy I, Strategy II also includes elastic transformation, such as pin cushion transformation and barrel transformation. Deformation of original images is beneficial to increasing robustness and the promotion of the final result. After data augmentation, a  $400 \times 400$  region is randomly cropped from the original image as input.

### 5.3. Evaluation

The evaluation method is the same as the competition requires. Three indicators are used to evaluate the performance on test A and test B. Indicators assess detection results, segmentation performance and shape similarity respectively. The final score is the summation of six rankings and the smaller



the better. Since image amounts of test A and test B have a significant difference in quantity, we not only calculate the rank sum as the host of MICCAI 2015 Gland Segmentation Challenge Contest demands, but we also list the weighted rank sum. We calculate the weighted average of three evaluation criteria on test set A and test set B. Since the images in test A account for 3/4 of the test set and images in test B account for 1/4, the weighted rank sum is calculated as:

$$WeightedRS = 3/4 \sum testARank + 1/4 \sum testBRank. \quad (10)$$

The program for evaluation is given by the MICCAI 2015 Gland Segmentation Challenge Contest (Sirinukunwattana et al., 2017). The first criterion for evaluation is the  $F_1$  score, which reflects gland detection accuracy. The segmented glandular object of True Positive (TP) is the object that shares more than 50% of areas with the ground truth. Otherwise, the segmented area will be determined as a False Positive (FP). Objects of ground truth without corresponding prediction are considered as False Negatives (FN).

$$F1 \quad Score = \frac{2 \cdot Precision \cdot Recall}{Precision + Recall} \quad (11)$$

$$Precision = \frac{TP}{TP + FP} \quad (12)$$

$$Recall = \frac{TP}{TP + FN} \quad (13)$$

Dice is the second criterion for evaluating segmentation performance. The dice index of the whole image is

$$D(G, S) = \frac{2(|G \cap S|)}{|G| + |S|}, \quad (14)$$

of which G represents the ground truth and S is the segmented result. Unfortunately, it is not able to differentiate instances of the same class. As a result, an object-level dice score is employed to evaluate segmentation results. The definition is as follows:

$$D_{object}(G, S) = 1/2 \left[ \sum_{i=1}^{n_S} w_i D(G_i, S_i) + \sum_{j=1}^{n_G} \tilde{w}_j D(\tilde{G}_j, \tilde{S}_j) \right], \quad (15)$$

$$w_i = \frac{|S_i|}{\sum_{j=1}^{n_S} |S_j|}, \quad (16)$$

$$\tilde{w}_i = \frac{|\tilde{G}_i|}{\sum_{j=1}^{n_G} |\tilde{G}_j|}. \quad (17)$$

$n_S$  and  $n_G$  are the numbers of instances in the segmented results and the ground truth.

Shape similarity reflects the performance on morphology likelihood which plays a significant role in gland instance segmentation. Hausdorff distance is exploited to evaluate shape similarity. To assess glands respectively, the index of Hausdorff distance deforms from the original formation:

$$H(G, S) = \max \left\{ \underset{x \in G}{\sup} \underset{y \in S}{\inf} \|x - y\|, \underset{y \in S}{\sup} \underset{x \in G}{\inf} \|x - y\| \right\}, \quad (18)$$

to the object-level formation:

$$H_{object}(S, G) = 1/2 \left[ \sum_{i=1}^{n_S} w_i H(G_i, S_i) + \sum_{i=1}^{n_G} \tilde{w}_i H(\tilde{G}_i, \tilde{S}_i) \right], \quad (19)$$

where

$$w_i = \frac{|S_i|}{\sum_{j=1}^{n_S} |S_j|}, \quad (20)$$

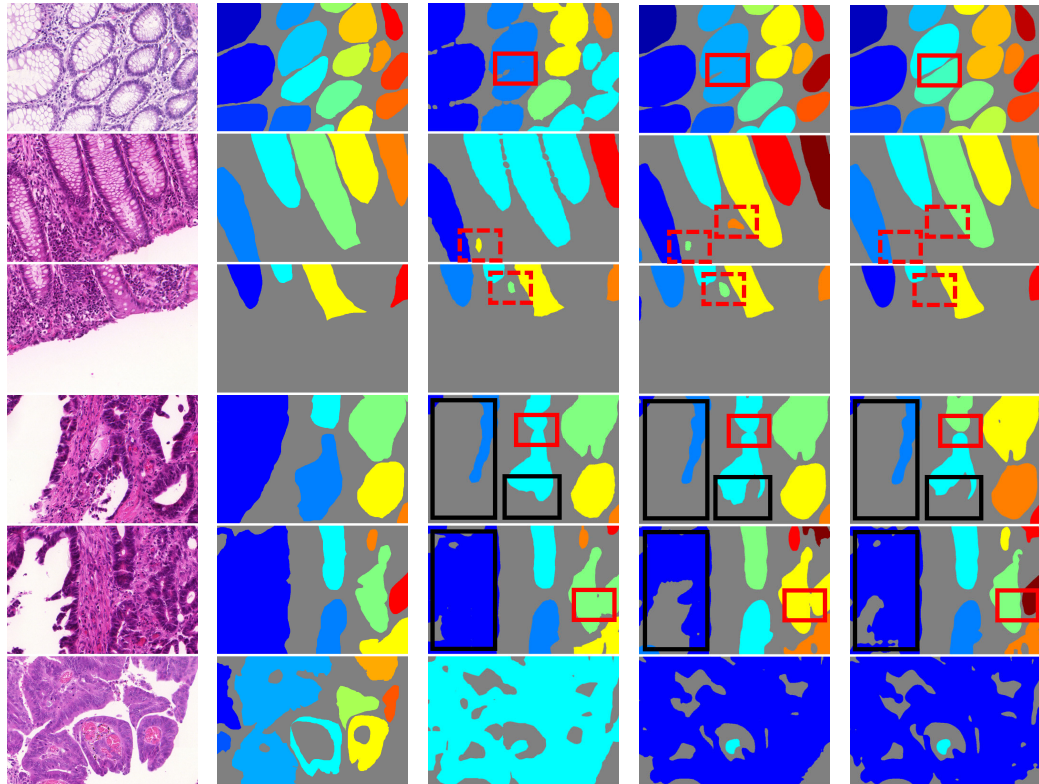
$$\tilde{w}_i = \frac{|\tilde{G}_i|}{\sum_{j=1}^{n_G} |\tilde{G}_j|}. \quad (21)$$

Similar to the object-level dice, index  $n_S$  and  $n_G$  represent instances of segmented objects and the ground truth.

#### 5.4. Result and Discussion

Table 1 lists results of our proposed algorithm, FCN, dilated FCN and other participants on datasets provided by the MICCAI 2015 Gland Segmentation Challenge Contest.

In the table, RS and WRS denote rank sum and weighted rank sum respectively. We rearrange the scores and ranks in this table. Our method outranks FCN, dilated FCN and other participants based on both rank sum and weighted rank sum.



(a) original image (b) ground truth (c) FCN (d) dilated FCN (e) our algorithm

Figure 6: From left to right: original image, ground truth, results of FCN (Long et al., 2015), FCN with dilated convolution and the proposed algorithm. Compared to FCN and dilated FCN, most adjacent glandular structures are separated (as shown inside the red solid boxes) which indicates that our algorithm accomplishes instance segmentation. Besides, our algorithm is able to correctly judge the small isolated area as non-gland area (as shown inside the red dotted boxes). However, a few glands that are broken apart escape the detection of our model (as shown inside the black boxes). The bad performance in the last row is due to the fact that in most samples the white area is recognized as cytoplasm while in this sample, the white area is the background.

Compared to FCN and dilated FCN, our algorithm obtains better scores which is convincing evidence that our work is more effective in solving instance segmentation problems in histological images. Though dilated FCN performs better than FCN as the dilated convolution process has less pooling and covers larger receptive fields, our algorithm combines region, location and edge information to achieve higher scores in the dataset. The reason our algorithm ranks higher is because most adjacent glandular structures have been separated, which is more beneficial to meet the evaluation index of instance segmentation, while in FCN and dilated FCN they are not. Comparison results are illustrated in Fig. 6.

Ranks of test A are generally higher than test B due to the inconsistency of data distribution. In test A, most images are normal ones while test B contains a majority of cancerous images which are more complicated in shape and larger in size. Hence, a larger receptive field is required in order to detect cancerous glands. However, before we exploit dilated convolution, the downsampling layer not only gives the network a larger receptive field but also makes the resolution of the feature map decrease, thus it deteriorates the segmentation results. Dilated convolution empowers the convolutional neural network with a larger receptive field with fewer downsampling layers. Our multichannel algorithm enhances performance based on the dilated FCN by adding two channels - edge detection and object detection.

Since the differences between background and foreground in histopathological images are small (3th row of Fig. 6), FCN and dilated FCN sometimes predict the background pixel as gland, raising the false positive rate. The multichannel algorithm abates the false positive by adding pixel context while

Method	F <sub>1</sub> Score				ObjectDice				ObjectHausdorff				RS	WRS
	Part A		Part B		Part A		Part B		Part A		Part B			
	Score	Rank	Score	Rank	Score	Rank	Score	Rank	Score	Rank	Score	Rank		
FCN (Long et al., 2015)	0.788	11	0.764	4	0.813	11	0.796	4	95.054	11	146.2478	4	45	27.75
dilated FCN (Chen et al., 2015)	0.854	9	0.798	2	0.879	6	0.825	2	62.216	9	118.734	2	30	19.5
<b>Ours</b>	0.893	3	<b>0.843</b>	<b>1</b>	<b>0.908</b>	<b>1</b>	<b>0.833</b>	<b>1</b>	<b>44.129</b>	<b>1</b>	<b>116.821</b>	<b>1</b>	8	4.5
CUMedVision2 (Chen et al., 2016)	<b>0.912</b>	<b>1</b>	0.716	6	0.897	2	0.781	8	45.418	2	160.347	9	28	9.5
ExB3 (Sirinukunwattana et al., 2017)	0.896	2	0.719	5	0.886	3	0.765	9	57.350	6	159.873	8	33	13.75
ExB2 (Sirinukunwattana et al., 2017)	0.892	4	0.686	9	0.884	4	0.754	10	54.785	3	187.442	11	41	15.75
ExB1 (Sirinukunwattana et al., 2017)	0.891	5	0.703	7	0.882	5	0.786	5	57.413	7	145.575	3	32	16.5
Frerburg2 (Ronneberger et al., 2015)	0.870	6	0.695	8	0.876	7	0.786	6	57.093	4	148.463	6	37	17.75
Frerburg1 (Ronneberger et al., 2015)	0.834	10	0.605	11	0.875	8	0.783	7	57.194	5	146.607	5	46	23
CUMedVision1 (Chen et al., 2016)	0.868	7	0.769	3	0.867	10	0.800	3	74.596	10	153.646	7	40	23.5
CVIP Dundee	0.863	8	0.633	10	0.870	9	0.715	11	58.339	8	209.048	13	59	27.25
LIB	0.777	12	0.306	14	0.781	12	0.617	13	112.706	13	190.447	12	76	37.5
CVML	0.652	13	0.541	12	0.644	14	0.654	12	155.433	14	176.244	10	75	39.25
vision4GlaS	0.635	14	0.527	13	0.737	13	0.610	14	107.491	12	210.105	14	80	39.5

\* RS is the abbreviation for rank sum and WRS is the abbreviation for weighted rank sum.

Table 1: Performance in Comparison to Other Methods

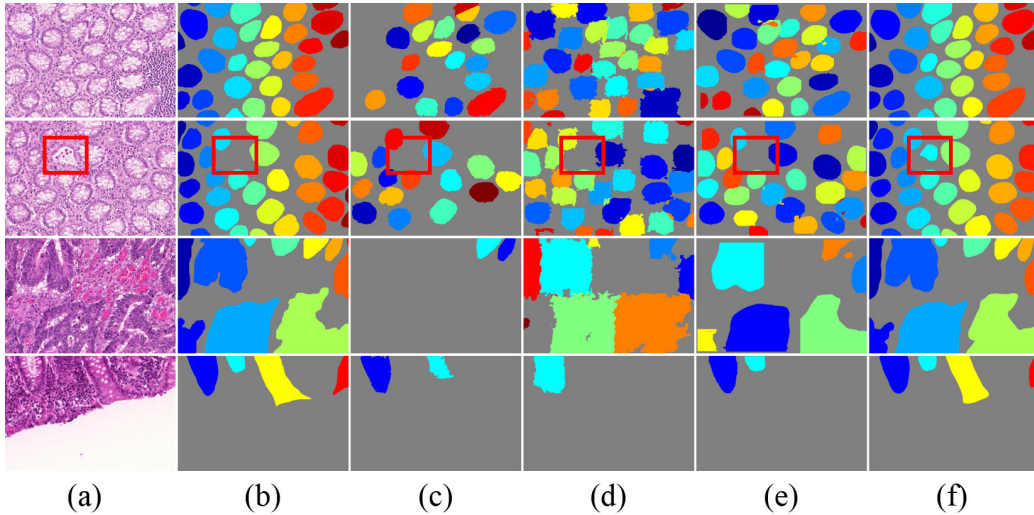


Figure 7: From (a) to (f): original image, ground truth, results of SDS (Hariharan et al., 2014), Hypercolumn (Hariharan et al., 2015), MNC (Dai et al., 2016b) and the proposed algorithm. Different color regions represent different gland instances. SDS, Hypercolumn and MNC all perform masking inside bounding boxes produced by object detection, which causes the coarse boundary of gland instances and even neglects some glands. In the second column, one gland instance is missed by manual labeling but our algorithm successfully detects its location and segments it with relatively complete shape, yet SDS, Hypercolumn and MNC fail to detect this gland (as shown inside of the red boxes).

predicting object location.

Compared to CUMedVision1 (Chen et al., 2016), CUMedVision2 (Chen et al., 2016) adds edge information which improves the results of test A but those of test B deteriorate. Our method improves results of test A and test B after combining edge and location context.

However, white regions in gland histopathological images are of two kinds: 1) cytoplasm; and 2) no cell or tissue (background). The difference between these two is that cytoplasm usually appears surrounded by nuclei or other stained tissue. In the image of the last row in Fig. 6, glands encircle some white regions with no existence of cell or tissue causing the algorithm to mistake them for cytoplasm. As for images of the 4th and 5th row in Fig. 6, glands are split when cutting images, which is the reason that cytoplasm is

mistaken for background.

**Comparison with instance segmentation methods** Currently, methods suitable for instance segmentation of natural scene images predict instances based on detection or proposal, such as SDS (Hariharan et al., 2014), Hypercolumn (Hariharan et al., 2015) and MNC (Dai et al., 2016b). One problem with this logic is its dependence on the precision of detection or proposal. If the object or a certain pixel of an object escapes the detection, it will evade the subsequent segmentation as well. Besides, the segmentation being restricted to a certain bounding box will have little access to context information hence it impacts the result. Under the condition of bounding boxes overlapping one another, which instance the pixel in the overlapping region belongs to cannot be determined. The overlapping area falls into the category of the nearest gland in our experiment. The experiment results are presented in Fig. 7.

To further demonstrate the defect of the cascade architecture, we design a baseline experiment. We first perform gland detection and then segment gland instances inside bounding boxes. There is a shallow network (same as the fusion network) combining foreground segmentation and edge detection information to generate the final result. Configurations of all experiments are set the same as our method. Results are shown in Table 2 and less effective than the proposed algorithm.

Method	$F_1$ Score		ObjectDice		ObjectHausdorff	
	Part A	Part B	Part A	Part B	Part A	Part B
HyperColumn (Hariharan et al., 2015)	0.852	0.691	0.742	0.653	119.441	190.384
MNC (Dai et al., 2016b)	0.856	0.701	0.793	0.705	85.208	190.323
SDS (Hariharan et al., 2014)	0.545	0.322	0.647	0.495	116.833	229.853
BOX->dilated FCN (Chen et al., 2015)+EDGE3	0.807	0.700	0.790	0.696	114.230	197.360
OURS	<b>0.893</b>	<b>0.843</b>	<b>0.908</b>	<b>0.833</b>	<b>44.129</b>	<b>116.821</b>

Table 2: Comparison with instance segmentation methods

## 5.5. Ablation Experiment

### 5.5.1. Data Augmentation Strategy

Data augmentation contributes to performance enhancement and overfitting elimination. We observe through experiments that adequate transformation of gland images is beneficial to training. This is because glands naturally form in various shapes and cancerous glands are more different in morphology. Here we evaluate the effect on results of the foreground segmentation channel using Strategy I and Strategy II (as shown in Table 3).

Strategy	Method	$F_1$ Score		ObjectDice		ObjectHausdorff	
		Part A	Part B	Part A	Part B	Part A	Part B
Strategy I	FCN (Long et al., 2015)	0.709	0.708	0.748	0.779	129.941	159.639
	dilated FCN (Chen et al., 2015)	0.820	0.749	0.843	0.811	79.768	131.639
Strategy II	FCN (Long et al., 2015)	0.788	0.764	0.813	0.796	95.054	146.248
	dilated FCN (Chen et al., 2015)	<b>0.854</b>	<b>0.798</b>	<b>0.879</b>	<b>0.825</b>	<b>62.216</b>	<b>118.734</b>

Table 3: Data Augmentation Strategy comparison

### 5.5.2. Plausibility of Channels

In convolutional neural networks, the main purpose of downsampling is to enlarge the receptive field, but this comes at a cost of decreased resolution and information loss of original data. Feature maps with low resolution increase the difficulty of upsample layer training. The representational ability of feature maps is reduced after upsampling and further leads to inferior segmentation results. Another drawback of downsampling is the space invariance it introduces while segmentation is space sensitive. The inconsistency between downsampling and image segmentation is obvious. Dilated convolution empowers the convolutional neural network with larger receptive field with less downsampling layers.

The comparison between segmentation performances of FCN with and without dilated convolution shows its effectiveness in enhancing segmentation precision. The foreground segmentation channel with dilated convolution improves the performance of the multichannel algorithm. So does the fusion stage with dilated convolution.

Pixels belonging to the edge occupy an extremely small proportion of the whole image. The imbalance between edge and non-edge poses a significant barrier to network training that may lead to non convergence. Edge dilation can alleviate the imbalance and improve edge detection precision.

To prove that these three channels truly improve instance segmentation performance, we conduct the following two baseline experiments: a) we launch a foreground segmentation channel and an edge detection channel; b) we launch a foreground segmentation channel and an object detection channel. The results favor the three-channel algorithm.

Results from the experiments mentioned above are presented in Table 4.

Method	$F_1$ Score		ObjectDice		ObjectHausdorff	
	Part A	Part B	Part A	Part B	Part A	Part B
MC: FCN + EDGE1 + BOX	0.863	0.784	0.884	0.833	57.519	108.825
MC: FCN + EDGE3 + BOX	0.886	0.795	0.901	0.840	49.578	100.681
MC: dilated FCN + EDGE3 + BOX	0.890	0.816	<b>0.905</b>	0.841	47.081	107.413
DMC: FCN + EDGE3 + BOX	<b>0.893</b>	0.803	0.903	<b>0.846</b>	47.510	<b>97.440</b>
DMC: dilated FCN + EDGE3 + BOX	<b>0.893</b>	<b>0.843</b>	0.908	0.833	<b>44.129</b>	116.821
DMC: dilated FCN + EDGE1 + BOX	0.876	0.824	0.894	0.826	50.028	123.881
DMC: dilated FCN + BOX	0.876	0.815	0.893	0.808	50.823	132.816
DMC: dilated FCN + EDGE3	0.874	0.816	0.904	0.832	46.307	109.174

Table 4: Plausibility of Channels. We denote DMC as the fusion network with dilated convolution (Chen et al., 2015) and MC as the fusion network without dilated convolution. EDGE1 represents that edge label are not dilated while EDGE3 represents that edge label are dilated by a disk filter with radius of 3. BOX indicates that the method includes object detection (Ren et al., 2015). FCN (Long et al., 2015) and dilated FCN (Chen et al., 2015) indicates that the method includes foreground segmentation.

## 6. Conclusion

We propose a new algorithm called deep multichannel neural networks. The proposed algorithm exploits features of edge, region and location in a multichannel manner to generate instance segmentation. We observe state-of-the-art results on the dataset from the MICCAI 2015 Gland Segmentation Challenge. A series of baseline experiments are conducted to prove the superiority of this method.

In future work, this algorithm can be expanded to instance segmentation of other medical images.

## Acknowledgment

This work is supported by Microsoft Research under the eHealth program, the Beijing Natural Science Foundation in China under Grant 4152033, the Technology and Innovation Commission of Shenzhen in China under Grant shenfagai2016-627, the Beijing Young Talent Project in China, the Fundamental Research Funds for the Central Universities of China under Grant SKLSDE-2015ZX-27 from the State Key Laboratory of Software Development Environment in Beihang University in China.



## References

## References

- Cheikh, B.B., Bertheau, P., Racoceanu, D., 2016. A structure-based approach for colon gland segmentation in digital pathology, in: SPIE.
- Chen, H., Qi, X., Yu, L., Heng, P.A., 2016. Dcan: Deep contour-aware networks for accurate gland segmentation, in: CVPR.
- Chen, L.C., Papandreou, G., Kokkinos, I., Murphy, K., Yuille, A.L., 2015. Deeplab: Semantic image segmentation with deep convolutional nets, atrous convolution, and fully connected crfs, in: ICLR.
- Ciresan, D., Giusti, A., Gambardella, L.M., Schmidhuber, J., 2012. Deep neural networks segment neuronal membranes in electron microscopy images, in: NIPS.
- Dai, J., He, K., Li, Y., Ren, S., Sun, J., 2016a. Instance-sensitive fully convolutional networks, in: NIPS.
- Dai, J., He, K., Sun, J., 2016b. Instance-aware semantic segmentation via multi-task network cascades, in: CVPR.
- Dimopoulos, S., Mayer, C.E., Rudolf, F., Stelling, J., 2014. Accurate cell segmentation in microscopy images using membrane patterns. *Bioinformatics* , 2644–2651.
- Egger, J., 2013. Pcg-cut: graph driven segmentation of the prostate central gland. *PLoS one* , e76645.
- Fleming, M., Ravula, S., Tatishchev, S.F., Wang, H.L., 2012. Colorectal carcinoma: pathologic aspects. *Journal of gastrointestinal oncology* , 153–173.
- Girshick, R., 2015. Fast r-cnn, in: ICCV.
- Girshick, R., Donahue, J., Darrell, T., Malik, J., 2014. Rich feature hierarchies for accurate object detection and semantic segmentation, in: CVPR.
- Hariharan, B., Arbeláez, P., Girshick, R., Malik, J., 2014. Simultaneous detection and segmentation, in: ECCV.

- Hariharan, B., Arbeláez, P., Girshick, R., Malik, J., 2015. Hypercolumns for object segmentation and fine-grained localization, in: CVPR.
- Kainz, P., Pfeiffer, M., Urschler, M., 2015. Semantic segmentation of colon glands with deep convolutional neural networks and total variation segmentation. CS .
- Krizhevsky, A., Sutskever, I., Hinton, G.E., 2012. Imagenet classification with deep convolutional neural networks, in: NIPS.
- Lee, C.Y., Xie, S., Gallagher, P., Zhang, Z., Tu, Z., 2015. Deeply-supervised nets., in: AISTATS.
- Li, W., Manivannan, S., Akbar, S., Zhang, J., 2016. Gland segmentation in colon histology images using hand-crafted features and convolutional neural networks, in: ISBI.
- Long, J., Shelhamer, E., Darrell, T., 2015. Fully convolutional networks for semantic segmentation, in: CVPR.
- Naik, S., Doyle, S., Agner, S., Madabhushi, A., Feldman, M., Tomaszewski, J., 2008. Automated gland and nuclei segmentation for grading of prostate and breast cancer histopathology, in: ISBI.
- Naik, S., Doyle, S., Feldman, M., Tomaszewski, J., Madabhushi, A., 2007. Gland segmentation and computerized gleason grading of prostate histology by integrating low-, high-level and domain specific information, in: MIAAB.
- Nguyen, K., Jain, A.K., Allen, R.L., 2010. Automated gland segmentation and classification for gleason grading of prostate tissue images, in: ICPR.
- Nguyen, K., Sabata, B., Jain, A.K., 2012a. Prostate cancer grading: Gland segmentation and structural features. PRL , 951–961.
- Nguyen, K., Sarkar, A., Jain, A.K., 2012b. Structure and context in prostatic gland segmentation and classification, in: MICCAI.
- Paul, A., Mukherjee, D.P., 2016. Gland segmentation from histology images using informative morphological scale space, in: ICIP.

- Ren, S., He, K., Girshick, R., Sun, J., 2015. Faster r-cnn: Towards real-time object detection with region proposal networks, in: NIPS.
- Ronneberger, O., Fischer, P., Brox, T., 2015. U-net: Convolutional networks for biomedical image segmentation, in: MICCAI.
- Sermanet, P., Eigen, D., Zhang, X., Mathieu, M., Fergus, R., LeCun, Y., 2013. Overfeat: Integrated recognition, localization and detection using convolutional networks, in: arXiv preprint arXiv:1312.6229.
- Simonyan, K., Zisserman, A., 2015. Very deep convolutional networks for large-scale image recognition, in: ICLR.
- Sirinukunwattana, K., Plum, J.P., Chen, H., Qi, X., Heng, P.A., Guo, Y.B., Wang, L.Y., Matuszewski, B.J., Bruni, E., Sanchez, U., et al., 2017. Gland segmentation in colon histology images: The glas challenge contest. *MIA* , 489–502.
- Sirinukunwattana, K., Snead, D.R., Rajpoot, N.M., 2015. A stochastic polygons model for glandular structures in colon histology images. *TMI* , 2366–2378.
- Tosun, A.B., Gunduz-Demir, C., 2011. Graph run-length matrices for histopathological image segmentation. *TMI* , 721–732.
- Travis, W.D., Brambilla, E., Noguchi, M., Nicholson, A.G., Geisinger, K.R., Yatabe, Y., Beer, D.G., A, C.P., Riely, G.J., Schil, P.E.V., et al., 2011. International association for the study of lung cancer/american thoracic society/european respiratory society international multidisciplinary classification of lung adenocarcinoma. *Journal of Thoracic Oncology* , 244–285.
- Xie, S., Tu, Z., 2015. Holistically-nested edge detection, in: ICCV.
- Xu, Y., Li, Y., Liu, M., Wang, Y., Lai, M.L., Chang, E.I.C., 2016. Gland instance segmentation by deep multichannel side supervision, in: MICCAI.
- Yu, F., Koltun, V., 2016. Multi-scale context aggregation by dilated convolutions, in: ICLR.